

Article

Comparing Fuzzy Sets and Random Sets to Model the Uncertainty of Fuzzy Shorelines

Ratna Sari Dewi ^{1,2}, Wietske Bijker ^{1,*} and Alfred Stein ¹

¹ Faculty of Geo-information Science and Earth Observation (ITC), University of Twente, P.O. Box 217, 7500 AE Enschede; The Netherlands; r.s.dewi@utwente.nl (R.S.D); a.stein@utwente.nl (A.S.)

² Geospatial Information Agency (BIG), Jl. Raya Jakarta-Bogor Km. 46, Cibinong, Bogor 16911, Indonesia

* Correspondence: w.bijker@utwente.nl; Tel.: +31-534874203

Academic Editors: Deepak Mishra and Prasad S. Thenkabail

Received: 19 July 2017; Accepted: 21 August 2017; Published: 25 August 2017

Abstract: This paper addresses uncertainty modelling of shorelines by comparing fuzzy sets and random sets. Both methods quantify extensional uncertainty of shorelines extracted from remote sensing images. Two datasets were tested: pan-sharpened Pleiades with four bands (*Pleiades*) and pan-sharpened Pleiades stacked with elevation data as the fifth band (*Pleiades + DTM*). Both fuzzy sets and random sets model the spatial extent of shoreline including its uncertainty. Fuzzy sets represent shorelines as a margin determined by upper and lower thresholds and their uncertainty as confusion indices. They do not consider randomness. Random sets fit the mixed Gaussian model to the image histogram. It represents shorelines as a transition zone between *water* and *non-water*. Their extensional uncertainty is assessed by the covering function. The results show that fuzzy sets and random sets resulted in shorelines that were closely similar. Kappa (κ) values were slightly different and McNemar's test showed high p -values indicating a similar accuracy. Inclusion of the DTM (digital terrain model) improved the classification results, especially for roofs, inundated houses and inundated land. The shoreline model using *Pleiades + DTM* performed better than that of using *Pleiades* only, when using either fuzzy sets or random sets. It achieved κ values above 80%.

Keywords: fuzzy sets; random sets; possibility; probability; shorelines; uncertainty

1. Introduction

Remote sensing offers a practical and economical means for coastal research. A series of remote sensing images can be used, for example, for mapping the dynamics of wet grassland and vegetation patches [1], mapping depth and water quality [2], coastal erosion [3], and in particular shoreline mapping [4–6]. Instantaneous shoreline locations extracted from remote sensing images have become popular since mapping shorelines using ground survey and photogrammetry is costly. Several methods have been proposed, for example, using manual digitization [7], spectral indices extraction such as water and vegetation indices [8], active contour segmentation [6], band ratios [9], and image classification [10,11]. Most of these methods are based on hard classifications, and only a few considered soft classifications in the context of shoreline mapping [4,5,12]. A hard classifier allocates a pixel to one class only based on the highest similarity. Therefore, applying hard classification for shoreline mapping could be misleading, since a shoreline is defined as the interface between land and water surfaces with its position changing over time. As images only capture a shoreline at a particular instant, they convey various kinds of uncertainties. Riesch [13] mentioned that uncertainties may be inherent in the system or can arise from incomplete knowledge. This first type of uncertainty is classified as errors [14] or as indeterminate boundaries [15,16]. When a shoreline is clearly identified, the errors or the kind of indeterminate boundaries may arise, for example, during data processing and measurements. Meanwhile, the second type of uncertainty is divided into

vagueness and ambiguity [14]. A vague boundary inherently belongs to the nature of the shorelines, i.e., it is hardly possible to define the extent of shoreline objects such as coast land, water and their gradual transition. The ambiguity may arise owing to the difference in classification system and perception of shorelines.

A common approach to model the uncertainty of objects is based upon probability theory [17]. For example, the epsilon band [18] is applied to model positional uncertainties of geographical objects. In addition, random sets theory is applied to handle the uncertainty in spatial information, for example for the definition of geographical areas, in mathematical morphology and in geostatistics [19]. Fuzzy sets theory introduced by Zadeh provides a conceptual framework for solving representation and classification problems in an ambiguous environment by means of membership functions [20].

In this study, we focused on the similarity of fuzzy sets and random sets in modelling the uncertainty in shoreline locations. Fuzzy sets are sets or classes that allow partial memberships [21,22]. A fuzzy set is characterized by a membership function which assigns to each object a grade of membership in the range [0,1], with 0 representing the “non-membership” and 1 representing the “full-membership” of the set. Two ways are commonly distinguished to develop this membership function: the semantic import model (SIM) derived from expert knowledge, and the fuzzy c-means classifier (FCM). SIM is subjective in nature [23] since it is based on subjective perceptions of vague categories rather than on data in the given problem, i.e., by extending the crisp boundaries into a transition zone [24]. In contrast, FCM is obtained from a set of attribute data and results in an objective approach. It is a commonly used method to estimate the membership values. FCM was developed by Dunn [25] and generalized by Bezdek [26]. Fuzzy sets theory has been widely used in remote sensing i.e., for image classification [5,27–29]. Fuzzy sets were applied also in GIS, e.g., for developing spatial data models for vague objects and their topological relation [23,30–32].

A random set is a generalization of a random variable taking subsets as values. Random sets theory is an inherent part of probability theory [33–35]. We can estimate the probabilities whether a random set is included in a given set, i.e., core, support and α -level sets or not [19]. Random sets theory has been employed to develop image segmentation methods [36], to characterize varying geometrical shapes [37] and to quantify the extensional uncertainty of spatial objects such as road polygons [38] and wetlands [1].

The connection between fuzzy sets and random sets has been discussed in the past [39–42]. Random sets theory is a methodology to deal with the uncertainty of outcomes of random phenomena. Fuzzy sets theory describes the uncertainty associated with classification or the placement of an outcome in a given class due to imprecision [42]. Goodman et al. [17] stated that fuzzy sets are equivalent to a weak specification of random sets. Moreover, Zadeh argued that probability theory must be used together with fuzzy logic to enhance its effectiveness and both theories are complimentary rather than competitive [39]. Fuzzy sets and random sets can be related via the one-point covering function of random sets, defined as the probability that an element is covered by a random set. The membership function of fuzzy sets is then considered as the probability of a random set covering a point [17,43,44].

The objective of this research is to compare the performance of fuzzy sets and random sets in shoreline mapping. In this case, *water* and *non-water* pixels were used as proxies to determine the shoreline features extracted from remote sensing images. The comparison between both methods is implemented using two types of images: original Pleiades and the combination of Pleiades with an airborne LIDAR altimetry data.

2. Methodology

2.1. Study Area

The study was conducted in an area situated along the north coast of Central Java, Indonesia (Figure 1). It is 4.6×4.2 km, or 4618×4262 pixels. The central point of the area is at Geographical coordinates $6^{\circ}56'S$ and $110^{\circ}29'E$.

The study site has an average slope of less than 5.0% and elevation of less than 5.0 m above mean sea level (MSL). From 30-year tidal data, the average tidal range of this location was 1.0 m (−0.5 to +0.5 m) [45]. The area has a mixed semi-diurnal tide with two high tides and two low tides with various heights. Tidal floods occur regularly in line with tidal cycles. Land subsidence with a rate approximately 6.0 cm year^{−1} [46] aggravates the severity of the flooding. Furthermore, the threat becomes even higher by the rise of sea level in Indonesia with an average of 0.6 cm year^{−1} [47].

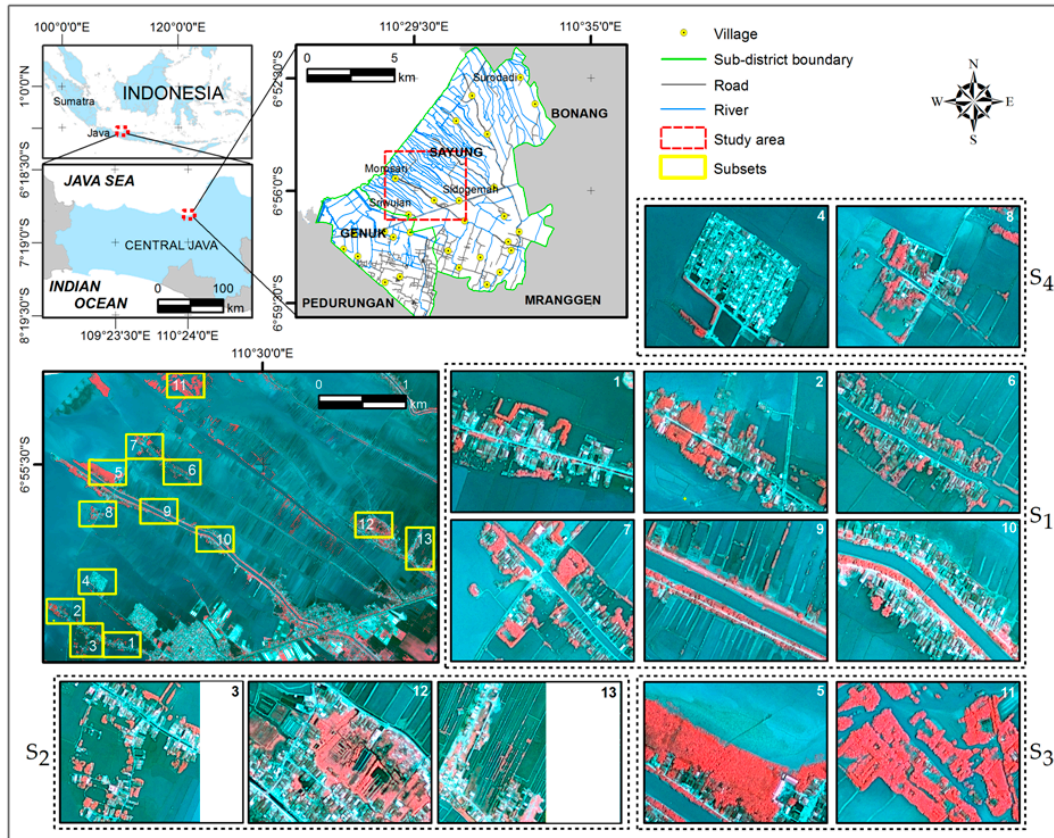


Figure 1. The study area, located in Sayung sub-district, Central Java Province, Indonesia. It is presented here as a false colour composite of a Pleiades image with red colour representing the vegetation, bluish green showing water area, and greyish and white pixels showing the built-up area. Yellow rectangles represent several the selected sites for this work, and black-dashed rectangles show four groups of subsets.

The site is a typical tidal area with a high density of rivers. In the past, it included extensive fishponds and rice fields [48] and the rivers were used for irrigations purposes. Rural settlements are found along the riverbanks or adjacent to the shorelines. Four villages, Bedono, Sriwulan, Sidogemah and Purwosari, are located in the study area, with population sizes equal to approximately 3500, 12,500, 7000 and 6300 inhabitants, respectively [49].

Since 1990s the productive fishponds and rice fields have been submerged and abandoned as swamp areas [50,51] leading to shoreline changes [4]. The area is prone to frequent inundations at high tide [52,53]. Several measures have been taken to minimize their impact, for example creation of dykes along the drainage system near the settlements, dredging the drainage channels, elevating roads and house floors, and building a permeable dam as sediment traps [54].

2.2. Dataset

We used a high resolution Pleiades image and elevation data. Water level observed from a nearby tide station at the time of image acquisition was also used. Those three data sources were provided by the Indonesia Geospatial Information Agency (BIG).

The image was acquired on 27 February 2013 at the lowest tides (the water level was 0.17 m below MSL). Table 1 shows the characteristics of the Pleiades image used.

Table 1. The characteristics of Pleiades image used.

Acquisition Date	27 February 2013
Acquisition time	03:04 UTC
Incidence angle (deg)	13.66
Sun elevation (deg)	62.51
Resolution (m)	0.5 (pan-sharpened product)
Bands (μm)	blue (0.43–0.55), green (0.50–0.62), red (0.59–0.71), NIR (0.74–0.94)
Map projection	UTM WGS84

The image is a pan-sharpened ortho product obtained in standard processing level at which pan-sharpening, radiometric and geometric corrections were applied by the image provider.

The DTM was created from Lidar data recorded in August 2014. The data are in UTM projection and elevations are in meters referenced to the Earth Gravitational Model 2008 (EGM 2008). The mission report [55] states that the DTM data have a pixel size of 1.0 m, a vertical accuracy of ± 0.17 m (linear error at 90% confidence, LE90), and a horizontal accuracy of ± 0.22 m (circular error at 90% confidence, CE90).

2.3. Pre-Processing

The DTM was combined with the Pleiades imagery to improve the quality of the classification. The DTM data and Pleiades image must be pre-processed before they can be combined. First, the Geoid-based DTM data needed to be adjusted, so that it coincided with local MSL. In the study area, the Geoid and MSL differ as much as 1.34 m [56]. Second, the DTM data were linearly stretched to map its original elevation range (−1.34 to 4.0 m) to the 16-bit range of Pleiades image. Third, the histogram minimum method [57] was applied to the image and the average filter was applied in 3×3 window size to reduce the image variance. Fourth, the Pleiades image was co-registered and resampled to match the DTM data.

For comparison of the methods, we prepared two types of datasets: (a) pan-sharpened Pleiades with four bands (referred to as *Pleiades*); and (b) pan-sharpened Pleiades with four bands that were stacked with the DTM as the fifth band (referred to as *Pleiades + DTM*). We created 13 subsets and grouped them into four groups (Figure 1), denoted as S_{a-b} as the name of subsets; a is the group number ($a = 1, \dots, 4$), and b is the subset number ($b = 1, \dots, 13$). Each subset consists of 423×282 pixels, except S_{2-3} , which consists of 374×381 pixels and S_{2-13} , which has 317×478 pixels. We grouped the subsets based on land cover similarities;

- S_1 is a mix of settlements and vegetation. This group consists of six subsets. They have a similar land orientation, stretching from northwest to southeast direction indicating rural settlements with a strip land surrounded by inundated fishponds. Rivers with various widths divide each island into two sides and small roads are found on either sides of the river. Rural settlements are mostly concentrated alongside the roads with sparse vegetation coverage.
- S_2 is a mix of settlement and vegetation with more complex composition. Small rivers are clearly seen in S_{2-3} and S_{2-12} . Fishponds with irregular shapes are visible at the northern part of S_{2-12} and S_{2-13} .
- S_3 is dominated by vegetation coverage. Rural settlements are visible in S_{3-5} along the river side and a wide muddy area can be found in the northern part of the subset close to the mangrove area.
- S_4 shows rural settlements surrounded by inundated fishponds. The settlements are protected by concrete embankment.

2.4. Modelling Shoreline Using Fuzzy Sets

2.4.1. FCM Classification

Unsupervised FCM was applied as the clustering algorithm [26] to estimate membership values. It separates the datasets into two classes allowing each pixel to have a membership value to multiple classes. The membership values (μ) range from 0 to 1, and add up to 1 for each pixel. In this work, the membership values of the classification follow the trapezoidal membership function [5].

FCM classification has a parameter c specifying the number of classes, and m specifying fuzziness. Bezdek, et al. [26] stated that values of m between 1.5 and 3.0 produced good results while Deer and Eklund [58] used $m = 1.6$. In our previous study using Landsat images, we found that $m = 1.7$ produced an accurate fuzzy classification. In this study, we investigated values of m from 1.1 to 3.0 in steps of 0.1 in to identify the optimal value. We also investigated a c value from 2 to 4 in order to find the optimal number of classes. In addition, we determined the cluster validity index from Xie and Beni [59] as:

$$XB = \frac{\sum_{i=1}^c \sum_{k=1}^N \mu_{ix}^2 \|V_i - X_x\|^2}{N \min_{ix} \|V_i - X_x\|^2} \quad (1)$$

XB refers to the compactness and separation validity function of fuzzy partition of the dataset $X = (1, 2, \dots, N)$, where $V_i (i = 1, 2, \dots, c)$ is the centroid of class i , N is the number of pixels (or data points), and μ_{ix} is the membership of pixel x to class i .

After clustering, membership images were compiled for each class. We labelled one of the two membership images as belonging to the *water class* by using the near infrared (NIR) band of Pleiades. The water label was given to the class which has the minimum value of the class mean in the near infrared band [5].

2.4.2. Image Segmentation

The possible shoreline location was determined by generating a margin or transition zone between classes *water* and *non-water*. We applied a similar approach [5], by defining a threshold range obtained from parameter estimation in the subsets. We applied thresholding to create crisp boundaries of the transition zone determined by lower (t_1) and upper thresholds (t_2). The class *water* C_w was defined as:

$$C_w = \begin{cases} 1 & \text{if } \mu_{wx} \geq t \\ 0 & \text{otherwise} \end{cases} \quad (2)$$

where μ_{wx} is the membership to *water*, and t is threshold value. We investigated values of t from 0.1 to 0.9 in steps of 0.1 to estimate the optimal threshold value.

2.4.3. Uncertainty Estimation

The uncertainty of deriving fuzzy shoreline was estimated by a measure of confusion index CI for each pixel as follows [15]:

$$CI = 1 - (\mu_{ix1} - \mu_{ix2}) \quad (3)$$

where μ_{ix1} refers to the first highest membership and μ_{ix2} denotes the second highest membership. The CI values range from 0 to 1. If the value approaches 1, it means the difference in membership value between the first and the second highest membership is small. The uncertainty of the pixel to belong to the class with the largest membership is high.

2.5. Modelling Shoreline by Random Sets

2.5.1. Parameter Estimation of Random Sets

Let the intensity of an image I within a window W be denoted as $f: W \rightarrow [0,1]$. Each pixel $x \in W$ has an intensity value $f(x) \in [0,1]$. The intensity function f can be interpreted as a collection of

sets = $\{x \in W, R \in [0,1]: f(x) \geq R\}$. F becomes a random set when R is a random variable. The distribution of a random set is determined by f and the random variable R [1].

The thresholding was chosen to model the shoreline from the *water* membership image. Thresholding is a process to separate pixels from an image into regions (or clusters) based on their intensity. Usually this segmentation process is based on the image histogram [60]. If the image is composed of regions with clear separation in its histogram, the histogram is usually bimodal with a deep valley. In that case, the bottom of the valley is taken as the threshold for foreground and background separation. However, the choice of threshold is not an easy task due to the existence of uncertain area in between the two peaks of the histogram. There are various methods to find the optimal threshold between the foreground and the background [1,61]. In this study, we consider the uncertain area, the transition zone between the foreground and background as the third class, *shoreline*, with intensity values in the interval $[t_1, t_2]$, where $0 \leq t_1 \leq t_2 \leq 1$ (Figure 2). We consider shoreline as the transition zone between water as the foreground and the coastal land as the background. We aim to extract the extent of *shoreline* and model it as a random set to quantify its extensional uncertainty.

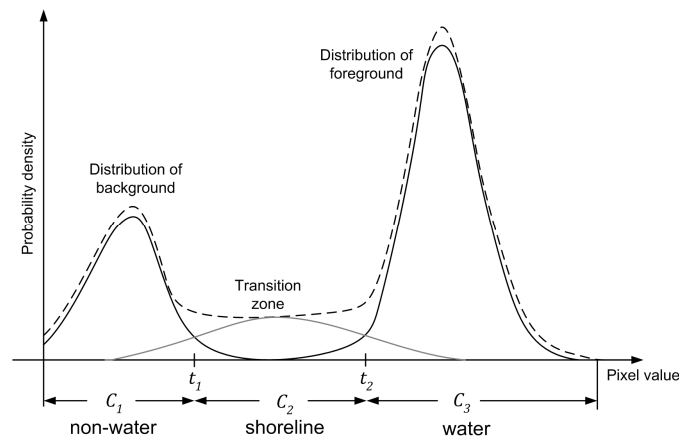


Figure 2. Density functions of shoreline object and related mixed Gaussian model.

The critical part of creating the random sets model is to generate realizations that characterize its distribution. To obtain these realizations, the probability distribution of R was determined and random numbers in the transition zone $[t_1, t_2]$ were generated as multiple thresholds. We chose the Gaussian distribution [1,61], based on the assumption that pixel values close to the object boundary have a higher probability to be labelled as the boundary than pixels at a distance.

A mixed Gaussian model was used to fit a density distribution to the image histogram and to determine the transition zone $[t_1, t_2]$ (Figure 2). When using multi-temporal images for shoreline mapping, each image has a different histogram reflecting a different proportion of transition zones. An image recorded during a low tide has a broader transition zone than an image recorded at a high tide. Hence, we chose the mixed Gaussian model with three components: the distributions of *water*, *non-water*, and *shoreline* as the transition zone.

Let the three classes be denoted as *non-water* (C_1), *shoreline* (C_2) and *water* (C_3). We assumed that the intensity of pixels which belong to class C_i , $i \in \{1, 2, 3\}$ follows the Gaussian distribution. C_i has the Gaussian distribution $C_i \sim N(M_i, \Sigma_i)$ with mean M_i , standard deviation Σ_i and density function $(\sqrt{2\pi\Sigma_i})^{-1} \exp\left[-\frac{1}{2}(z - M_i)^2/\Sigma_i^2\right]$ in a one-dimensional model. The density function of I is the mixed density distribution of C_i :

$$d(z) = d(z; \theta_i, M_i, \Sigma_i) = \sum_{i=1}^3 \theta_i N(M_i, \Sigma_i)(z) \tag{4}$$

where $z = f(x)$, θ_i is the weight coefficient for C_i and $\sum_{i=1}^3 \theta_i = 1$. It is assumed that $M_1 < M_2 < M_3$. The lower limit of the *shoreline* is to be determined at t_1 where $\theta_1 N(M_1, \Sigma_1)(t_1) = \theta_2 N(M_2, \Sigma_2)(t_1)$, and the upper limit at t_2 where $\theta_2 N(M_2, \Sigma_2)(t_2) = \theta_3 N(M_3, \Sigma_3)(t_2)$. In this way, we

identify three classes as presented in Figure 2: *non-water* (C_1): $f(x) < t_1$, *shoreline* (C_2): $t_1 \leq f(x) \leq t_2$, and *water* (C_3): $f(x) > t_2$. The transition interval $[t_1, t_2]$ is determined by tuning the weight of the *shoreline* component. For example, suppose that the thresholds 0.4, 0.5, and 0.6 were adopted for *shoreline* hard classification, and then we investigated an interval around these values, to find the optimal threshold interval for random sets.

2.5.2. Modelling the Extent of Shoreline by Random Sets

We generated n random numbers from the distribution $R \sim N(M_2, \Sigma_2)$ in $[t_1, t_2]$. This results into different realizations of a random set O_i, \dots, O_n by thresholding the *water* membership image using R_i, \dots, R_n as the multiple thresholds: $O_i = \{x \in W, i \in \{1, \dots, n\}, R_i \in [t_1, t_2]: f(x) \geq R_i\}$. We investigated the optimal value of n ($n = 10, \dots, 300$) in steps of 10. Intuitively, a value closer to the optimal n should be more reliable and the variance of random sets Γ becomes stable as n increases. For each n , the covering function $Pr_\Gamma(x)$ can then be determined including the core, median, support and level sets. We provided a curve for the core area as a function of n values. If the difference of two standardized core area between two successive n (denoted as d_i) is small (e.g., in the range -1 to $+1$), we accepted this n as the optimal n .

The idea of the generation of random sets is that the extent of segmented shoreline objects should be sensitive to the variance of the parameter in the threshold when we extracted objects with a large extensional uncertainty. By slightly changing the threshold values R_i, \dots, R_n , we obtained a set of objects O_i, \dots, O_n and construct a random set Γ . For example, for $n = 100$ and threshold interval $[0.3, 0.7]$, this means that we generate 100 thresholds to slice the membership image and make samples as binary maps. Each sample is a realization of focal element O_i of random sets Γ . The focal elements are regions which are subsets of W : $O_i \in \mathcal{P}(W)$. If the random set is constructed by n focal elements with equal probability, then $u_i = 1/n$. We need to estimate the covering function $Pr_\Gamma(x)$ to measure the probability of pixel x being covered by random sets. The covering function characterizes the distribution of random sets Γ . The covering function $Pr_\Gamma(x)$ at point x equals $P(\Gamma \cap \{x\} \neq \emptyset) = P(x \in \Gamma)$. It can be described by focal elements O_i with corresponding uncertainty assignments u_i , indicated as a collection of pairs $\{O_i, u_i\}, i \in (1, \dots, n)$ [38]. The covering function of random sets can be estimated by [1,38]:

$$Pr_\Gamma(x) = \frac{1}{n} \sum_{i=1}^n I_{O_i}(x), x \in W \tag{5}$$

where I_{O_i} is the indicator function of $O_i, i \in (1, \dots, n)$: $I_{O_i} = \begin{cases} 1, & x \in O_i \\ 0, & x \notin O_i \end{cases}$.

Figure 3a illustrates a simple example for covering function estimations of random sets with equal uncertainty assignments reflected by equal interval u_i . Figure 3b shows the covering function values at six pixels derived by Equation (5). Table 2 provides the statistical parameters of random sets [62].

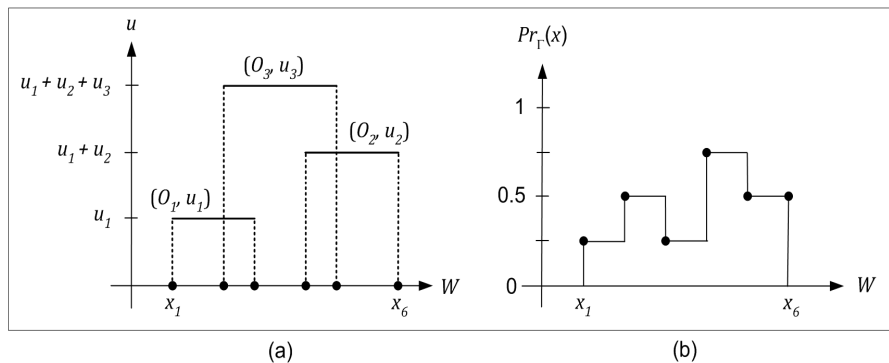


Figure 3. Focal elements with their equal uncertainty assignments $u_1 = u_2 = u_3$ to construct a realization of random sets (a); and covering function of the random sets (b). These figures are adapted from Zhao et al. [62].

Table 2. The statistical parameter of random sets.

Definition	Equations
The α -level set: to describe the spatial distribution of the varying sizes of Γ	$\Gamma_\alpha = \{x \in R^2, 0 \leq \alpha \leq 1: Pr_\Gamma(x) \geq \alpha\}$
The core set: to describe the certain part of Γ	$\Gamma_1 = \{x \in R^2: Pr_\Gamma(x) = 1\}$
The median set: to describe the 0.5-level set	$\Gamma_{0.5} = \{x \in R^2: Pr_\Gamma(x) = 0.5\}$
The support set: to describe the possible part of Γ	$\Gamma_0 = \{x \in R^2: Pr_\Gamma(x) > 0\}$
The mean area of Γ	$EA(\Gamma) = \int_{R^2} Pr_\Gamma(x) dx$
The mean set of Γ	$\Gamma_m = \{x \in R^2, 0 \leq \alpha_m \leq 1: Pr_\Gamma(x) \geq \alpha_m\}$
The set-theoretic variance	$\Gamma_v(x) = \frac{1}{n} \sum_{i=1}^n (I_{o_i}(x) - Pr_\Gamma(x))^2$
The sum of variance SV	$SV = \int_{\Gamma_0} \Gamma_v(x) dx$
The coefficient of variation CV	$CV = \frac{\int_{\Gamma_0} \sqrt{\Gamma_v(x)} dx}{\int_{\Gamma_0} Pr_\Gamma(x) dx}$

2.6. Validation and Comparing Classification Performance

To quantify the accuracy of each model, we used the error matrix to estimate the κ (kappa) values. In this case, we produced a hardened FCM using $t = 0.5$ and the median set $\Gamma_{0.5}$. We compared the performance of both approaches using two input images (*Pleiades* and *Pleiades + DTM*).

Reference data were derived from the 0.5 m *Pleiades* image acquired in 2013. Using stratified random sampling, approximately 138 points were randomly selected for each subset. A visual interpretation approach was performed to distinguish a land cover class for each selected point.

To test the significance of the difference between: a) fuzzy sets and random sets; b) *Pleiades* and *Pleiades + DTM*, we performed McNemar’s test [63–65]. McNemar’s test is based on confusion matrices that are 2 by 2 in dimension. The null hypothesis stated that both input images produced similar accuracy. The test is based on chi-square statistics at the 95% level of confidence, and computed as follows:

$$\chi^2 = \frac{(f_{12} - f_{21})^2}{(f_{12} + f_{21})} \tag{6}$$

where f_{12} denotes number of cases that are incorrectly classified by the first method or the first image but correctly classified by the second method or the second image, and f_{21} denotes number of cases that are correctly classified by the first method or the first image but incorrectly classified by the second method or the second image.

3. Results

3.1. Modelling Shoreline Using Fuzzy Sets

3.1.1. Parameter Estimation of FCM Classification

Figure S1 shows the κ values when we estimated c and m values for all subsets of the *Pleiades + DTM* image. For low m (e.g., $m = 1.1$ – 1.6), classifications show a comparable κ for all thresholds, and the highest κ was obtained for $c = 2$, while by setting a high m ($m = 2.0$ – 3.0), high κ values were obtained only for certain t values. For example, when we set $m = 1.5$ and $c = 2$, high κ were obtained for $t = 0.2$ – 0.8 while for $m = 3$ and $c = 3$, high κ were only obtained for $t = 0.2$. In this case, for a high m value, the choice of t becomes more sensitive. In addition, Table S1 shows the cluster validity measures as an alternative approach to determine the number of classes for FCM classification. From the results, $c = 2$ obtained the minimum values for all m which indicates a partition in which all clusters are overall compact, and separate from each other. Based on both approaches in estimating the suitable number of classes for FCM classification, we decided $c = 2$ was the optimal number of classes for further image processing steps.

Figure S2 shows the results of threshold range estimation when we set a constant c ($c = 2$) for various m . We can see that $t = 0.5$ gave a highest κ value for all subsets while the threshold range 0.3–0.7 provided high κ values. High values of m resulted in a low κ value, especially at a low t ($t < 0.3$) and a high t value ($t > 0.6$). Given the fact that the threshold range 0.3–0.7 produced high κ values, we selected those values as the threshold range at which the boundary between water and land can probably be distinguished.

In Figure S2, we can also see that $m = 1.5$ and $m = 1.6$ are comparable as indicated by the stability of κ value, whereas, for $m > 1.6$, the choice of t becomes more sensitive. Given the results, we chose $m = 1.6$ as the optimal m value for FCM.

3.1.2. Hardened FCM and Accuracy Comparison

Figures 4 and 5 show the comparison of thresholding results for hardened FCM at $t = 0.5$ for both input images. The inclusion of DTM data has improved the classification results. In Figure 4, an example is presented at which roofs (*non-water*) were correctly classified by *Pleiades + DTM*, but were classified incorrectly by *Pleiades*. The classification improvement also can be seen from Figure 5 provides an example in which inundated land was clearly identified by *Pleiades + DTM*.

Table 3 shows the comparison of the accuracy between *Pleiades* and *Pleiades + DTM*. For all subsets, *Pleiades + DTM* outperformed *Pleiades*. Table S2 presents the significance of the different accuracies given by both images. Seven of the tests show significant improvement of the *Pleiades + DTM* over the *Pleiades*, as shown by very low p -values, whereas, few results have similar accuracies, as shown by p -value ≥ 0.05 .

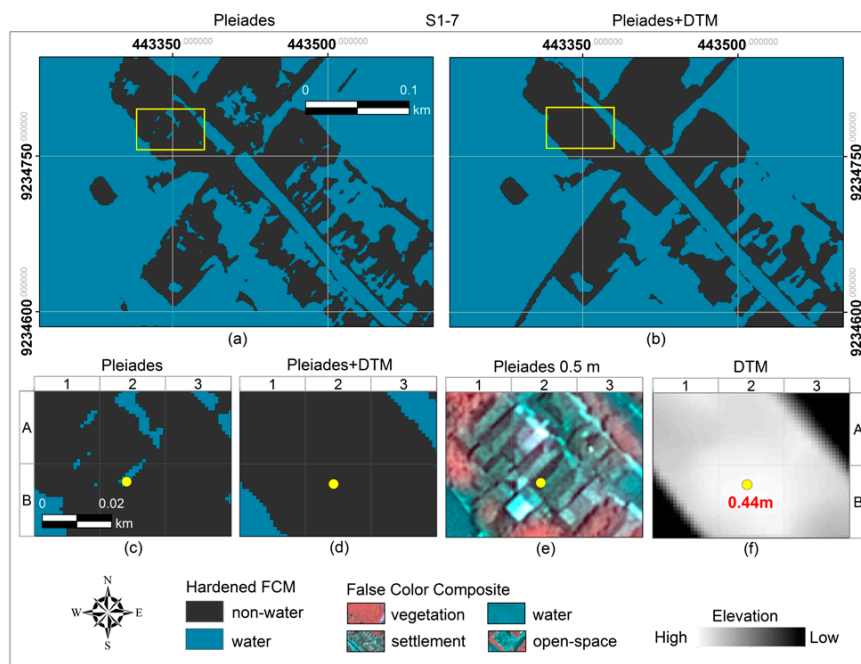


Figure 4. Comparison of the fuzzy classification results between: *Pleiades* (a,c); and *Pleiades + DTM* (b,d). *Pleiades* 0.5 m (e); and elevation data (f) are displayed to interpret the attribute of yellow points. In (c,d), we can see that *Pleiades* misclassified pixels as water instead of roofs (*non-water*), as can be seen in (e).

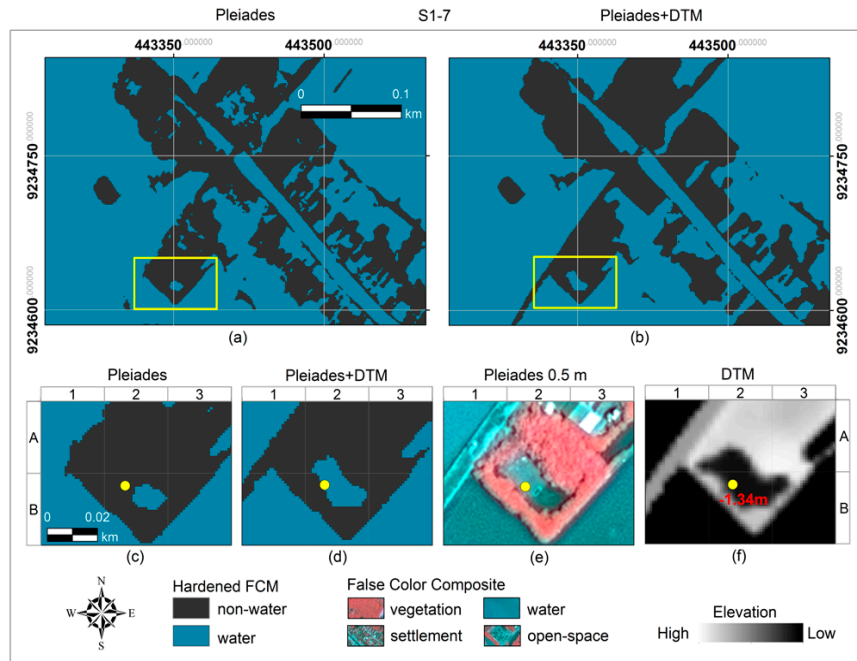


Figure 5. An example of inundated land that was: incorrectly classified by *Pleiades* (a,c); and classified successfully by *Pleiades + DTM* (b,d). *Pleiades* 0.5 m (e); and elevation data (f) are presented to interpret the yellow points.

Table 3. The accuracy comparison between *Pleiades* and *Pleiades + DTM* using FCM classification with thresholding ($c = 2, m = 1.6, t = 0.5$). The inclusion of DTM in classifications clearly improved the classification results. S_{a-b} : the name of subsets, a is the group number ($a = 1, \dots, 4$) and b is the subset number ($b = 1, \dots, 13$).

Subset	<i>Pleiades</i>	<i>Pleaides + DTM</i>
S_{1-1}	0.77	0.86
S_{1-2}	0.62	0.86
S_{1-6}	0.76	0.88
S_{1-7}	0.48	0.84
S_{1-9}	0.56	0.87
S_{1-10}	0.74	0.88
S_{2-3}	0.74	0.91
S_{2-12}	0.74	0.87
S_{2-13}	0.78	0.87
S_{3-5}	0.50	0.82
S_{3-11}	0.74	0.89
S_{4-4}	0.65	0.88
S_{4-8}	0.67	0.81

3.1.3. Fuzzy Shoreline and Uncertainty Estimation

Figure 6 shows an illustration of shoreline margin with fuzziness generated by setting $t = 0.3$ as the lower t and $t = 0.7$ as the upper t by using *Pleiades + DTM* (for other results, see Figure S3). In this figure, the shoreline (in light green colour) represents the transition zone between *water* (in blue colour) and *non-water* (in black colour). The combination of the shoreline image and the confusion index is provided in Figure 6d. In this figure, a wider shoreline indicates a wider gradual transition between *water* and *non-water* representing a more gently sloping beach or muddy coastal area, while a narrow shoreline indicates a steeper sloping beach.

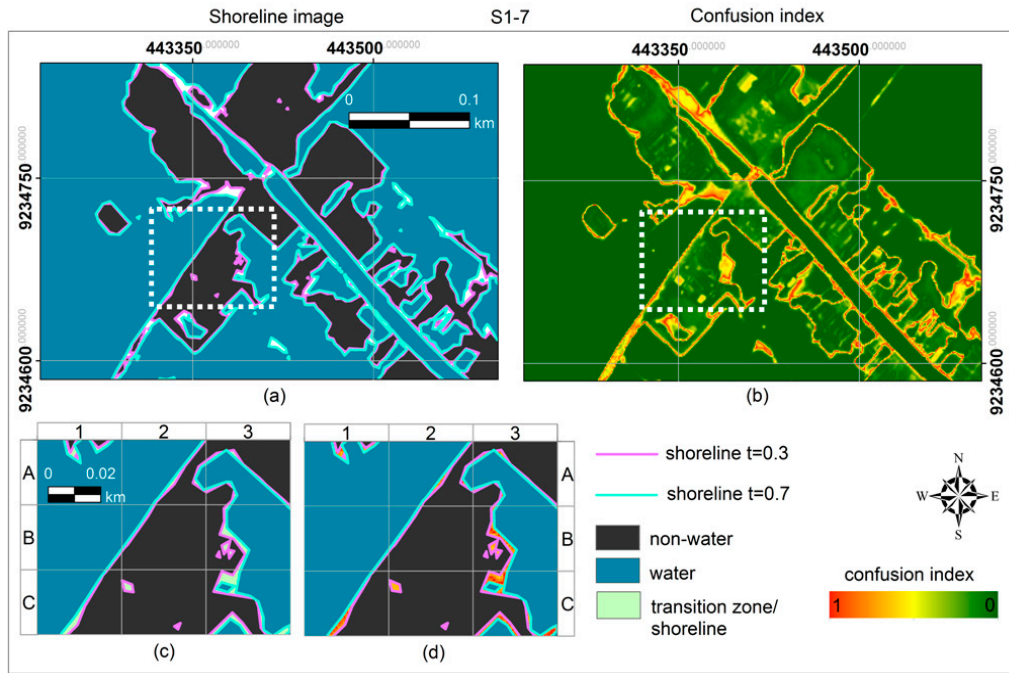


Figure 6. The shoreline as the transition zone between *water* and *non-water* (a); the fuzziness of the shoreline is represented by the confusion index denoting the uncertainty of pixels to be classified to the largest membership (b); zooming into the white-dashed rectangle sites (c); and shoreline image with fuzziness represented by the confusion index (d).

3.2. Modelling Shoreline by Random Sets

3.2.1. Parameter Estimation Results

Table S3 show the results of parameter n and threshold interval estimation of random sets with the related κ values estimated from the $\Gamma_{0.5}$. In Table S3 and Figure 7, it can be seen that threshold interval = 0.3–0.7 generally produced the highest κ value.

We plotted the curves of the Γ_1 area for four subsets by setting the selected threshold interval = 0.3–0.7 (see Figures 8 and S4). From these curves, we can assess the optimal n at which we obtained a stabile Γ_1 area. Each subset has a different n to reach a stabile Γ_1 area, which might be influenced by the land cover characteristics of the study area. In Figure 8, the curve of S_{4-4} reached the highest n value to achieve the stability of the Γ_1 area, whereas S_{2-12} reached the lowest n .

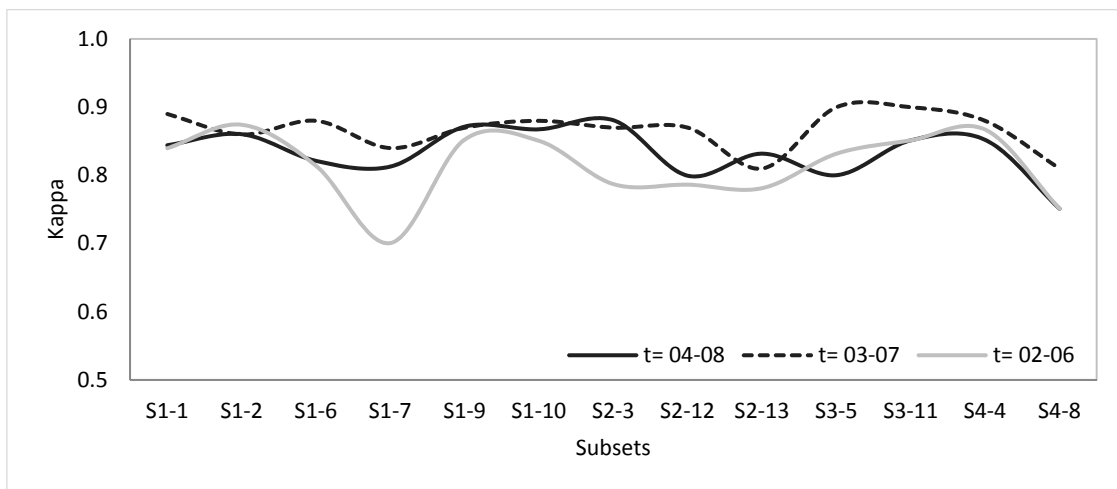


Figure 7. Estimation of threshold interval for random sets based on the optimal n selected for each subset. Threshold interval = 0.3–0.7 generally produced the highest κ value. S_{a-b} : the name of subsets, a is the group number ($a = 1, \dots, 4$) and b is the subset number ($b = 1, \dots, 13$).

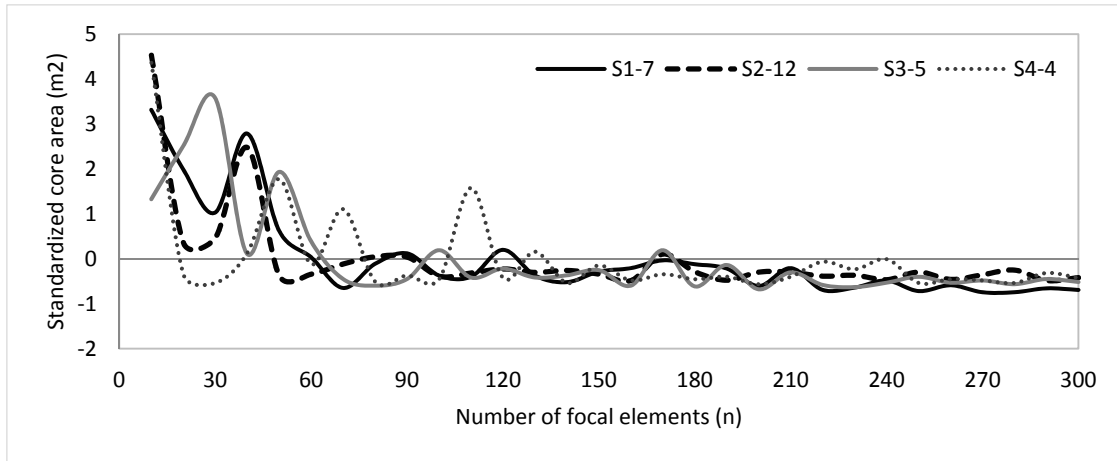


Figure 8. The curve of differences between two successive standardized core sets d_i . When d_i is in the range -1 to $+1$, we determined this n value for performing random sets (see notations in Figure 7 for the name of subsets).

3.2.2. Uncertainty Modelling of Shoreline Objects

Figure 9 shows some examples of binary images and the related covering functions that resulted from slicing water membership images determined by the optimal n (the other results can be seen in Figure S5). By slightly changing the threshold for μ_{wx} , we obtained binary maps as a realization of focal element O_i with various extents. From these focal elements, we constructed random sets by estimating the covering function, as can be seen in Figure 9f.

We plotted the area of focal elements to explore information on the extent of random sets (see Figure 10). From the plot in Figure 10, we can see that S_{2-12} , S_{2-13} , and S_{3-5} have the largest variance, whereas S_{4-4} , S_{1-10} and S_{1-9} have the smallest variance.

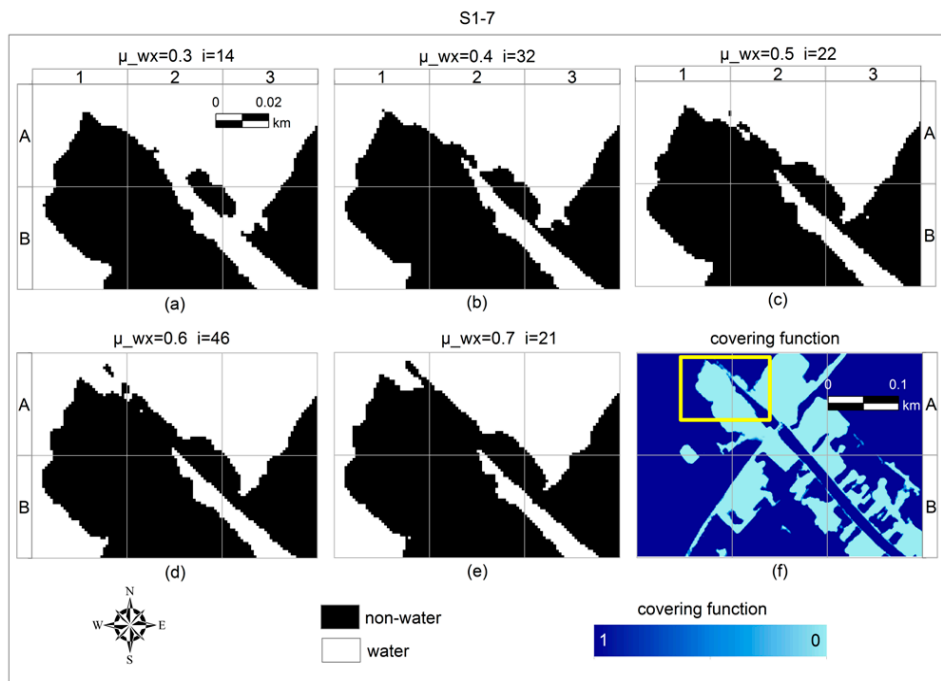


Figure 9. Samples of the random sets with various extents and their covering function. (a–e) Samples are at $\mu_{wx} = 0.3$ – 0.7 . Pixels in white indicate the *water* area and pixels in black indicate the *non-water* area. (f) The related covering functions, where 0 indicates a low probability and 1 indicates a high probability to be covered by the random sets. Various extents of focal elements at each binary map can be seen when zooming into the yellow rectangle site.

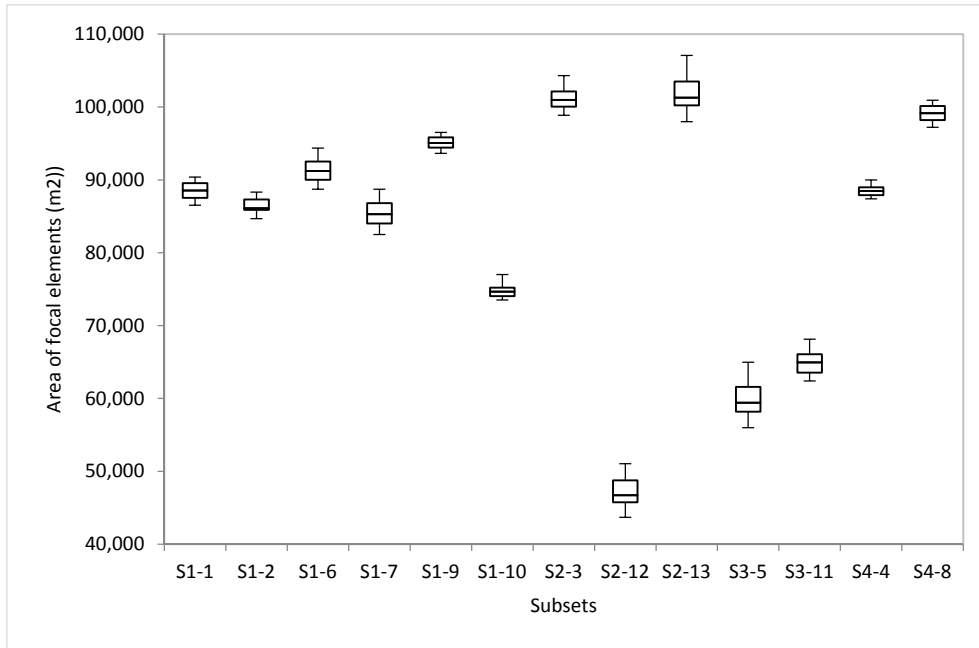


Figure 10. Statistical distribution of area of focal elements sampled from 13 random sets (see notations in Figure 7 for the name of subsets).

In Table 4, we can see that subset S_{4-4} has the lowest CV value. A lower CV indicates that the random sets have small Γ_v , reflecting a lower uncertainty. By checking the Pleiades image in Figure 1, it is obvious that S_{4-4} comprises a rural settlement with concrete roads. The settlement was protected by embankment from its surrounding open water. For an object with little uncertainty, the membership values are homogenous. Therefore, the resulting samples O_1, \dots, O_n have similar extents (see Figure 10 subset S_{4-4}). On the contrary, S_{2-12} has the highest CV value, which obviously indicates the highest uncertainty. For an object with a high uncertainty, the membership values are heterogeneous. Hence, the resulting samples O_1, \dots, O_n have various extents and are very sensitive to small variations in t value (see Figure 10 subset S_{2-12}).

In Figure 11a, the set-theoretic variance Γ_v is presented in grey scale values with light colour denoting high variations in uncertain transition zones and dark colour denoting low variations of *water* and *non-water* (the other results can be seen in Figure S6). For pixels inside Γ_1 or outside Γ_0 , Γ_v equals 0, whereas pixels close to the contours of Γ_1 or Γ_0 have Γ_v values in the range [0,1]. Figure 11b shows the contours of Γ_1 , Γ_m and Γ_0 of random sets. The yellow rectangle sites (1) in Figure 11a,b have a different extent implying that these sites have a wider, more gradual transition (see Figure 11c), mainly caused by the location close to the mangrove forest in a muddy area. For the yellow sites (2), however, the contours of Γ_1 , Γ_m and Γ_0 are similar and the segmentation boundaries show small variation (see Figure 11d).

More pixels with a non-zero Γ_v in the objects indicate a large uncertainty area. SV values are the largest for S_{2-12} , S_{2-13} , and S_{3-5} (see Table 4) because the number of pixels with non-zero Γ_v values in those subsets are the largest (see Figure S6). Subsets S_{1-9} , S_{4-4} and S_{4-8} have the smallest CV, which can be observed well in Figure S6 indicating a small number of pixels with a non-zero Γ_v .

The extent of the shoreline is represented by a random sets model in Figure 12 as an example of the representations of the core set Γ_1 , the support set Γ_0 , and the covering function $Pr_T(x)$ of random sets (see Figure S7 for other results). Figure 12a shows the Γ_1 (in blue pixels) representing the area that obviously belongs to water. Figure 12b displays the Γ_0 (in blue colour) indicating the possible part of the area that belongs to *water*, whereas the area outside this Γ_0 belongs to *non-water* (see black pixels in Figure 12d). The gradual changes in the transition zone representing the shoreline are represented by the set-theoretic variance Γ_v . Pixels with value close to 1 have a high variation indicating a high uncertainty, whereas, pixels with value close to 0 have a low variation indicating a low uncertainty (Figure 12d,e). A clear distinction exists between a narrow transition zone, for

example, which separates settlements and open water (Figure 12e, e.g., grid cells A2 and B2), and broad transition zones between open water and vegetation (Figure 12e, e.g., grid cells B3).

Table 4. The quantification of the extensional uncertainty of the all subsets (the SV is the sum of variance, and CV denotes the coefficient of variance). See notations in Table 3 for the name of subsets.

Subset	SV	CV
S_{1-1}	657	0.007
S_{1-2}	811	0.009
S_{1-6}	915	0.010
S_{1-7}	901	0.010
S_{1-9}	466	0.005
S_{1-10}	574	0.008
S_{2-3}	953	0.009
S_{2-12}	1525	0.032
S_{2-13}	1710	0.017
S_{3-5}	1490	0.025
S_{3-11}	883	0.014
S_{4-4}	441	0.005
S_{4-8}	580	0.006

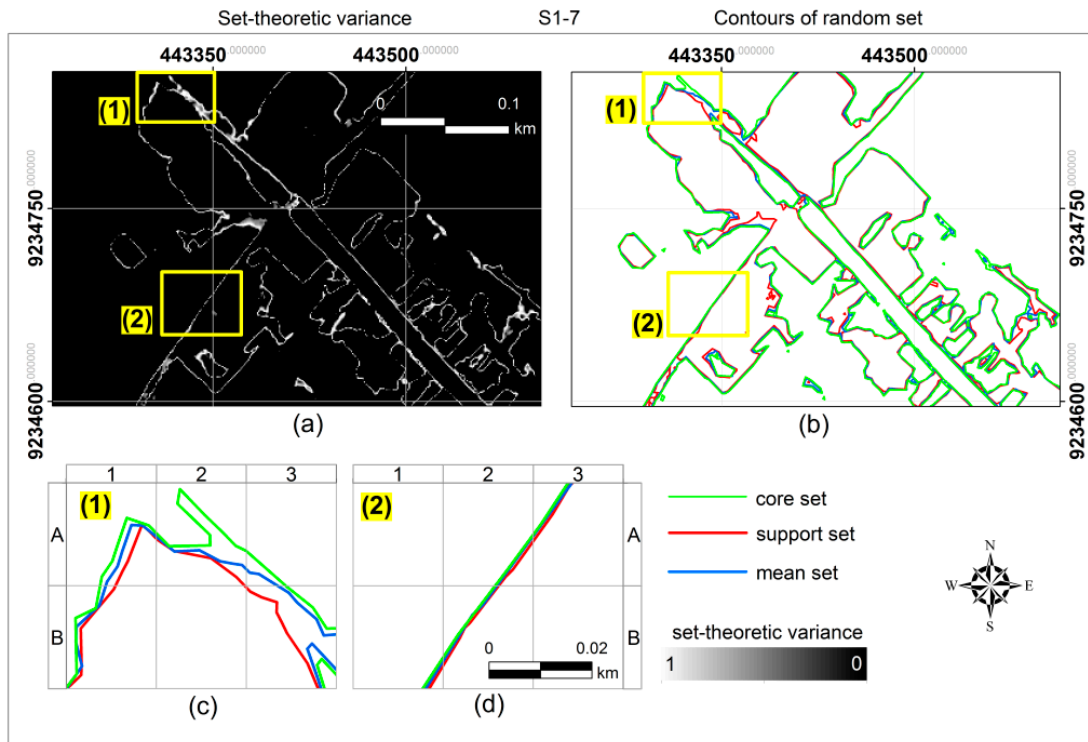


Figure 11. The set-theoretic variance (a); some examples of the contour of Γ_1 , $\Gamma_{0.5}$ and Γ_0 (b); and a detail representing the yellow rectangle sites as an example of contours with a broad variation (c); and contours with a small variation indicating a narrow shoreline (d).

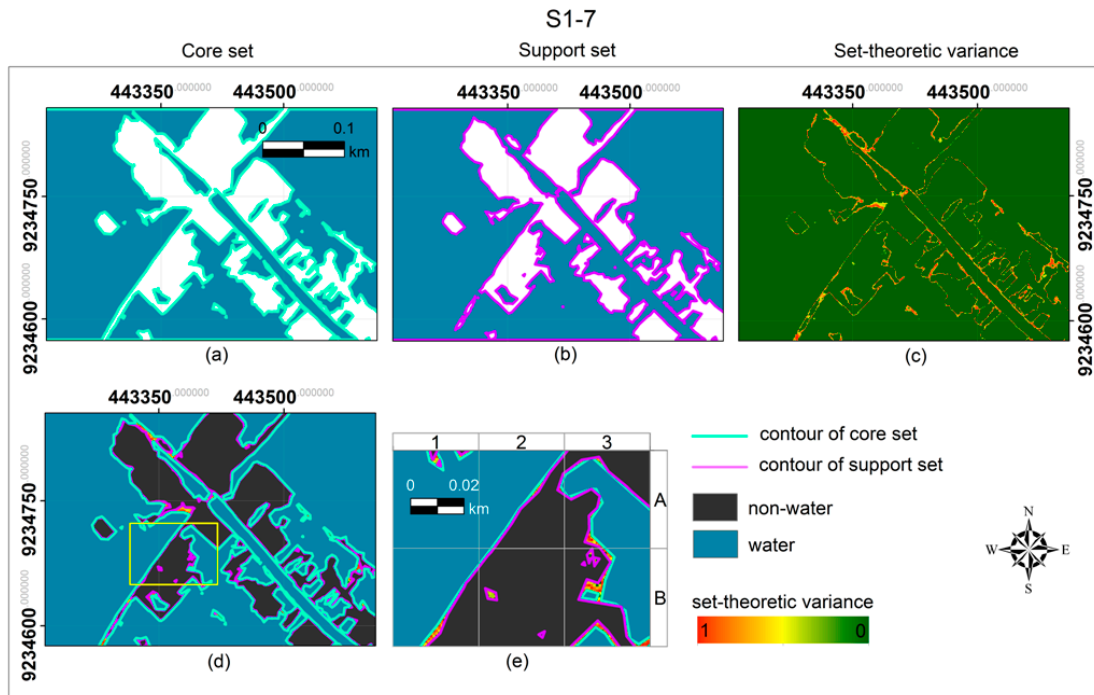


Figure 12. An example of a random set: the core set T_1 and its contour (a); the support set T_0 and its contour (b); the set-theoretic variance image (c); the transition zone between *water* and *non-water* represented by the set-theoretic variance values (d); and zoom-in to the yellow rectangle site (e).

3.2.3. Accuracy Assessment of Random Sets Results

Table 5 shows the comparison of accuracy between *Pleiades* and *Pleiades + DTM* by using random sets. Similar to fuzzy sets, using random sets, *Pleiades + DTM* outperformed *Pleiades*. McNemar’s test results of random sets using *Pleiades* and *Pleiades + DTM* are shown in Table S4. Seven of the subsets show significant improvement of the *Pleiades + DTM* over the *Pleiades* image, as shown by their very low *p*-values (see Table S4 subsets S_{1-1} , S_{1-2} , S_{1-7} , S_{1-9} , S_{1-10} , S_{3-5} , and S_{4-4}), whereas the rest of the results show that similar accuracies were obtained from both of them.

Table 5. The accuracy comparison between *Pleiades* and *Pleiades + DTM* by random sets (see notations in Table 3 for the name of subsets).

Subset	<i>Pleiades</i>	<i>Pleiades + DTM</i>
S_{1-1}	0.76	0.89
S_{1-2}	0.58	0.86
S_{1-6}	0.76	0.88
S_{1-7}	0.48	0.84
S_{1-9}	0.56	0.87
S_{1-10}	0.74	0.88
S_{2-3}	0.75	0.87
S_{2-12}	0.74	0.87
S_{2-13}	0.79	0.81
S_{3-5}	0.56	0.90
S_{3-11}	0.77	0.90
S_{4-4}	0.66	0.88
S_{4-8}	0.67	0.81

3.3. Comparing Classification Performance

Table S5 presents the McNemar's test results by fuzzy sets and random sets using *Pleiades* image. The table indicates that the methods agree on f_{22} and f_{11} but disagree on f_{12} and f_{21} cases. From the test results, we can see that p -values are relatively high (≥ 0.05) implying that both methods obtained a similar accuracy when using *Pleiades*.

Table S6 presents the McNemar's test results by fuzzy sets and random sets using *Pleiades + DTM* image as input data. From the test results, we can see that p -values are relatively high (≥ 0.05) implying that both methods obtained a similar accuracy when using *Pleiades + DTM*.

4. Discussion

This research compared two methods for handling the uncertainty of shorelines: fuzzy sets and random sets. Shoreline is a spatial object with inherent uncertainty that cannot be extracted effectively from satellite images by means of a crisp-based classification, since these methods ignore uncertain areas or gradual transition zones. This paper demonstrates that fuzzy sets and random sets produced comparable results for modelling the uncertainty of fuzzy shorelines. When using fuzzy sets, the same results can be achieved without taking randomness into account, as confirmed by Zadeh [39].

The κ accuracies from both fuzzy sets and random sets are slightly different (see Tables 3 and 5). In addition, the McNemar's test failed to reject the null hypothesis of equal performance of both methods by using either *Pleiades* or *Pleiades + DTM* (see Tables S5 and S6). Although fuzzy sets and random sets were not identical, shorelines resulted from both methods were close to each other (see Figures 6d and 12e) and neither could be considered more accurate, as confirmed by the literature [43,44]. This is probably related to the fact that each segmentation of random sets can be interpreted as a different interpretation of a fuzzy concept, since the multiple thresholds to generate the segments are selected among the possible interpretations [43]. Furthermore, Goodman argued that any given fuzzy sets is equal to one nested random set [44].

Both methods were successful in identifying the spatial extent of shorelines including their extensional uncertainties. Fuzzy sets present a shoreline as a margin derived from a crisp boundary determined by t values. Here, the extensional uncertainty of shoreline represented by a confusion index values implies that the shoreline can be detected with limited certainty. Through the confusion index, the presence of a gradual transition was distinguished when the values of an adjacent grid are very similar. When using random sets, a shoreline is presented as the third class, the transition zone between *water* and *non-water*. The extensional uncertainty of a shoreline was assessed by using the covering function of random sets and its statistical parameters (Γ_1 , Γ_m , Γ_0 and Γ_v). By using these parameters, we demonstrated that the randomness of segmentation parameters, i.e., multiple thresholds, has a different effect on extracted features when objects have different extensional uncertainties (see Figure 9). Moreover, there are other indicators such as SV and CV to summarize the size of extensional uncertainties. A high SV and CV indicate a high extensional uncertainty.

Fuzzy sets were applied by first estimating the membership function. In this study, we computed the membership value by performing FCM classification. On the one hand, this method is less subjective as compared to the semantic import model [24,66], while, on the other hand, the choice of values for c and m influence the results of the classification. In contrast, random sets as a probabilistic approach avoid user interference [34,67] in generating random sets.

The random sets model was combined with thresholding to model shorelines from water membership images. Here, the choice of n as the number of focal elements was critical. Improper threshold values R_1, \dots, R_n , from the worst n values in segmentation will result in errant segments. At low n , the Γ_1 area changed abruptly, and by the increasing of n values, the Γ_1 area reached its stability. In fact, by increasing n , we increase the chance to have optimal threshold values for segmentation of random sets. Performing random sets modelling with such large n values was computationally expensive. Comparing random sets to fuzzy sets, fuzzy sets were relatively computationally less expensive. However, the choice of optimal c , m , and t values for classification influences the results and requires a thorough investigation.

To model a shoreline using fuzzy sets, we need to adopt other concepts to quantify the extensional uncertainty of the shoreline, such as α -cut, shoreline as a margin, and fuzzy-crisp object [4,5,28], whereas a random sets approach through its covering function and statistical parameters directly quantifies the extensional uncertainty of shoreline without resorting to other concepts.

The integration of DTM data improved the results of both fuzzy sets and random sets. The integration of Pleiades and elevation has higher accuracy than Pleiades only. The additional DTM band leads to an improvement in the classification accuracy for roofs, inundated houses and inundated land. After this integration, roofs were clearly distinguished and separated from their surroundings (i.e., water and inundated soil). Usually, the ground close to the building location is slightly higher than its surroundings while water area or an inundated land clearly has a lower elevation. By using only Pleiades, it was difficult to discriminate dark roofs and water or inundated soil, since they are often have similar spectral characteristics. The ability to discriminate two similar characteristics is influenced by the number of spectral bands available. The other objects that were successfully classified from the addition of DTM were inundated houses and land. In this case, the elevation data help to identify the water area. In addition to the benefit given by addition of the DTM in the classification, a downside could be found as well, especially for tree objects. This is due to the time difference between Pleiades and DTM data of one and half years. In several locations, trees were submerged and finally no longer exist in newer data and these changes caused loss of accuracy. In this case, the use of DTM data that have the same date of acquisition as the remote sensing image is preferable.

5. Conclusions

In this paper, fuzzy sets and random sets are compared for shoreline detection. Both methods performed well in modelling the uncertainty of shorelines and had similar results when using either *Pleiades* or *Pleiades + DTM*.

Application of fuzzy sets produced a higher classification accuracy for *Pleiades + DTM* than for *Pleiades*. Similarly, for random sets, *Pleiades + DTM* gained a significant improvement over *Pleiades*. Considerable improvements were achieved for objects, e.g., roofs, inundated houses and yards. *Pleiades + DTM* achieved an accuracy above 80%, demonstrating that it provides a valuable data source for shoreline mapping. In the absence of elevation data, we may overestimate in particular the water area. The research further confirmed the need of DTM integration to remote sensing images to provide reliable and accurate shoreline mapping that may give benefit to coastal planners and managers. The proposed methods are to be further applied in other areas for future study. This will help to better understand how different condition of the area can influence the results and to upscale the methods to larger areas of land.

Supplementary Materials: The following are available online at www.mdpi.com/2072-4292/9/9/895/s1, Figure S1: The estimation results of c and m for FCM classification; Table S1: The cluster validity index showing the compactness and the separateness among all clusters (applied using $m = 1.6$); Figure S2: The estimation of threshold interval for $c = 2$ and various m values for FCM classification; Table S2: The results of McNemar's test showing the significance of the different accuracies given by *Pleiades* and *Pleiades + DTM* ($\alpha = 0.05$) in FCM classification with thresholding; Figure S3: The shoreline as the transition zone between *water* and *non-water* (Columns 1 and 5); confusion index images (Columns 2 and 6); zooming into the white-dashed rectangle sites (Columns 3 and 7); and shoreline images with fuzziness represented by the confusion index (Columns 4 and 8); Table S3: The optimal n selected for each threshold interval and the related κ values for generation of random sets; Figure S4: The curve of differences between two successive standardized core sets d_i ; Figure S5: Samples of the random sets with various extents and their covering functions; Figure S6: The set-theoretic variance and the contour of random sets; Figure S7: An example of random sets; the core set Γ_1 and its contour (Columns 1 and 5); the support set Γ_0 and its contour (Columns 2 and 6); the transition zone between *water* and *non-water* represented by the set-theoretic variance (Columns 3 and 7); and zooming into the yellow rectangle sites (Columns 4 and 8); Table S4: The results of McNemar's test showing the significance of the different accuracies given by *Pleiades* and *Pleiades + DTM* ($\alpha = 0.05$) in random sets; Table S5: The results of McNemar's test showing the significance of the difference given by fuzzy sets and random sets ($\alpha = 0.05$) by using *Pleiades*; Table S6: The

results of McNemar's test showing the significance of the difference given by fuzzy sets and random sets ($\alpha = 0.05$) using *Pleiades + DTM* data.

Acknowledgments: This study has been supported by the scholarship Program for Research and Innovation in Science and Technologies (RISET-PRO), Ministry of Research, Technology and Higher Education of Indonesia. The authors express their gratitude to Valentyn A. Tolpekin and John R. Bergado from the Faculty of Geo-information Science and Earth Observation (ITC), University of Twente for providing the script code for FCM, random sets, and cluster validity index.

Author Contributions: Ratna Sari Dewi had responsibility for conducting the research including writing the manuscript. Two other authors supervised the work, and revised the manuscript. All authors have read and approved the final manuscript.

Conflicts of Interest: The authors declare no conflict of interest.

References

1. Zhao, X.; Stein, A.; Chen, X.-L. Monitoring the dynamics of wetland inundation by random sets on multi-temporal images. *Remote Sens. Environ.* **2011**, *115*, 2390–2401.
2. Jay, S.; Guillaume, M. A novel maximum likelihood based method for mapping depth and water quality from hyperspectral remote-sensing data. *Remote Sens. Environ.* **2014**, *147*, 121–132.
3. Hereher, M.E. Mapping coastal erosion at the Nile Delta western promontory using Landsat imagery. *Environ. Earth Sci.* **2011**, *64*, 1117–1125.
4. Dewi, R.S.; Bijker, W.; Stein, A. Change Vector Analysis to Monitor the Changes in Fuzzy Shorelines. *Remote Sens.* **2017**, *9*, 147.
5. Dewi, W.S.; Bijker, W.; Stein, A.; Marfai, M.A. Fuzzy Classification for Shoreline Change Monitoring in a Part of the Northern Coastal Area of Java, Indonesia. *Remote Sens.* **2016**, *8*, 190.
6. Sukcharoenpong, A.; Yilmaz, A.; Li, R. An Integrated Active Contour Approach to Shoreline Mapping Using HSI and DEM. *IEEE Trans. Geosci. Remote Sens.* **2016**, *54*, 1586–1597.
7. Dewan, A.; Corner, R.; Saleem, A.; Rahman, M.M.; Haider, M.R.; Rahman, M.M.; Sarker, M.H. Assessing channel changes of the Ganges-Padma River system in Bangladesh using Landsat and hydrological data. *Geomorphology* **2017**, *276*, 257–279.
8. Ouma, Y.O.; Tateishi, R. A water index for rapid mapping of shoreline changes of five East African Rift Valley Lakes: An empirical analysis using Landsat TM and ETM+ Data. *Int. J. Remote Sens.* **2007**, *27*, 3153–3181.
9. Kuleli, T. Quantitative analysis of shoreline changes at the Mediterranean Coast in Turkey. *Environ. Monit. Assess.* **2010**, *167*, 387–397.
10. García-Rubio, G.; Huntley, D.; Russell, P. Evaluating shoreline identification using optical satellite images. *Mar. Geol.* **2015**, *359*, 96–105.
11. Taha, L.G.E.; Elbeih, S.F. Investigation of fusion of SAR and Landsat data for shoreline super resolution mapping: The Northeastern Mediterranean sea coast in Egypt. *Appl. Geomat.* **2010**, *2*, 177–186.
12. Muslim, A.M.; Foody, G.M.; Atkinson, P.M. Localized soft classification for super-resolution mapping of the shoreline. *Int. J. Remote Sens.* **2006**, *27*, 2271–2285.
13. Riesch, H. Levels of Uncertainty. In *Essentials of Risk Theory*; Roeser, S., Hillerbrand, R., Sandin, P., Peterson, M., Eds.; Springer Netherlands: Dordrecht, The Netherlands, 2013.
14. Fisher, P.F. Models of uncertainty in spatial data. *Geogr. Inf. Syst.* **1999**, *1*, 191–205.
15. Burrough, P.A.; van Gaans, P.F.M.; Hootsmans, R. Continuous classification in soil survey: Spatial correlation, confusion and boundaries. *Geoderma* **1997**, *77*, 115–135.
16. Schneider, M. Modeling spatial objects with undetermined boundaries using the realm/rose approach. In *Geographic Objects with Indeterminate Boundaries*; Burrough, P.A., Frank, A.U., Eds.; Taylor & Francis: London, UK, 1998; pp. 1–12.
17. Goodman, I.R.; Nguyen, H.T. *Uncertainty Models for Knowledge-Based Systems*; North Holland: Amsterdam, The Netherlands, 1985.
18. Skidmore, A.K.; Turner, B.F. Map Accuracy Assessment Using Line Intersect Sampling. *Photogramm. Eng. Remote Sens.* **1992**, *58*, 1453–1457.
19. Couso, I.; Dubois, D.; Sánchez, L. *Random Sets and Random Fuzzy Sets as Ill-Perceived Random Variables*; Springer: New York, NY, USA, 2014.

20. Zadeh, L.A. Fuzzy Sets. *Inf. Control* **1965**, *8*, 338–355.
21. Zadeh, L.A. PRUF a meaning representation language for natural languages. *Int. J. Mach. Stud.* **1978**, *10*, 395–460.
22. Tso, B.; Mather, P. *Classification Methods for Remotely Sensed Data*; CRC Press: Boca Raton, FL, USA, 2009.
23. Robinson, V.B. A Perspective on the Fundamentals of Fuzzy Sets and their Use in Geographic Information Systems. *Trans. GIS* **2003**, *7*, 3–30.
24. Cheng, T. Fuzzy Objects: Their Changes and Uncertainties. *Photogramm. Eng. Remote Sens.* **2002**, *68*, 41–49.
25. Dunn, J.C. A Fuzzy Relative of the ISODATA Process and Its Use in Detecting Compact Well-Separated Clusters. *Cybern. Syst.* **1973**, *3*, 32–57.
26. Bezdek, J.C.; Ehrlich, R.; Full, W. FCM: The fuzzy c-means clustering algorithm. *Comput. Geosci.* **1984**, *10*, 191–203.
27. Zhang, J.; Foody, G.M. A fuzzy classification of sub-urban land cover from remotely sensed imagery. *Int. J. Remote Sens.* **1998**, *19*, 2721–2738.
28. Cheng, T.; Molenaar, M.; Lin, H. Formalizing fuzzy objects from uncertain classification results. *Int. J. Geogr. Inf. Sci.* **2001**, *15*, 27–42.
29. Vlag, D.E.V.D.; Stein, A. Incorporating Uncertainty via Hierarchical Classification Using Fuzzy Decision Trees. *IEEE Trans. Geosci. Remote Sens.* **2007**, *45*, doi:10.1109/TGRS.2006.885403
30. Dilo, A.; By, R.A.D.; Stein, A. A system of types and operators for handling vague spatial objects. *Int. J. Geogr. Inf. Sci.* **2007**, *21*, 397–426.
31. Liu, K.; Shi, W.; Zhanga, H. A fuzzy topology-based maximum likelihood classification. *ISPRS J. Photogramm. Remote Sens.* **2011**, *66*, 103–114.
32. Schneider, M. Fuzzy Topological Predicates, Their Properties, and Their Integration into Query Languages. In Proceedings of the 9th ACM International Symposium on Advances in Geographic Information Systems, Atlanta, GA, USA, 9–11 November 2001; ACM Digital Library: Atlanta, GA, USA, 2001; pp. 9–14.
33. Matheron, G. *Random Sets and Integral Geometry*; John Wiley and Sons: New York, NY, USA, 1975.
34. Nguyen, H.T. *An Introduction to Random Sets*; Chapman & Hall/CRC: Boca Raton, FL, USA, 2006.
35. Molchanov, I. *Theory of Random Sets*; Springer: London, UK, 2005.
36. Epifanio, I.; Soille, P. Morphological Texture Features for Unsupervised and Supervised Segmentations of Natural Landscapes. *IEEE Trans. Geosci. Remote Sens.* **2007**, *45*, 1074–1083.
37. Stoyan, D.; Stoyan, H. *Fractals, Random Shapes and Point Fields: Methods of Geometrical Statistics*; John Wiley and Sons: Chichester, UK, 1994.
38. Zhou, L.; Stein, A. Application of random sets to model uncertainty of road polygons extracted from airborne laser points. *Comput. Environ. Urban Syst.* **2013**, *41*, 289–298.
39. Zadeh, L.A. Discussion: Probability Theory and Fuzzy Logic Are Complementary Rather Than Competitive. *Technometrics* **1995**, *37*, 271–276.
40. Nguyen, H.T.; Wu, B. Random and fuzzy sets in coarse data analysis. *Comput. Stat. Data Anal.* **2006**, *51*, 70–85.
41. Goodman, I.R.; Mahler, R.P.S.; Nguyen, H.T. *Mathematics of Data Fusion*; Springer: Dordrecht, The Netherlands, 1997.
42. Singpurwalla, N.D.; Booker, J.M. Membership Functions and Probability Measures of Fuzzy Sets. *J. Am. Stat. Assoc.* **2004**, *99*, 867–877.
43. Mahler, R.P.S. *Statistical Multisource-Multitarget Information Fusion*; Artech House: Norwood, MA, USA, 2007.
44. Goodman, I.R. Some New Results Concerning Random Sets and Fuzzy Sets. *Inf. Sci.* **1984**, *34*, 93–113.
45. BIG Online Tidal Prediction. Available online: <http://tides.big.go.id/> (accessed on 3 December 2016).
46. Chaussard, E.; Amelung, F.; Abidin, H.; Hong, S.-H. Sinking cities in Indonesia: ALOS PALSAR detects rapid subsidence due to groundwater and gas extraction. *Remote Sens. Environ.* **2013**, *128*, 150–161.
47. Sofian, I. *Scientific Basis: Analysis and Projection of Sea Level Rise and Extreme Event*; National Development Planning Agency: Bappenas, Indonesia, 2010.
48. Dames, T.W.G. *The Soils of East Central Java*; The General of Agricultural Research Station: Bogor, Indonesia, 1955.
49. BPS. *Regional Statistics of Sayung Subdistrict in 2015*; Central Bureau of Statistics of Demak Regency: Central Java, Indonesia, 2015.

50. Rondonuwu, C. The Sinking of Bedono. Available online: <https://www.ekuatorial.com/2010/11/the-sinking-of-bedono/#!/story=post-6051&loc=-1.625758360412755,119.43237304687499,4> (accessed on 2 August 2017).
51. Hartini, S. Flood Risk Modelling on Agricultural Area in the North Coastal Area of Central Java. Ph.D. Thesis, Gadjah Mada University, Yogyakarta, Indonesia, 2015.
52. Marfai, M.A.; King, L. Tidal inundation mapping under enhanced land subsidence in Semarang, Central Java Indonesia. *Nat. Hazards* **2008**, *44*, 93–109.
53. Harwitasari, D.; van Ast, J.A. Climate change adaptation in practice: People's responses to tidal flooding in Semarang, Indonesia. *J. Flood Risk Manag.* **2011**, *4*, 216–233.
54. Winterwerp, H.; Wesenbeeck, B.V.; Dalfsen, J.V.; Tonneijck, F.; Astra, A.; Verschure, S.; Eijk, P.V. A sustainable solution for massive coastal erosion in Central Java. In *Discussion Paper; Deltares-Wetland International: Delft, The Netherlands*, 2014; pp. 1–45.
55. Anonymous. *Control Points (GCP and ICP) Measurement Completion Report*; Indonesia Geospatial Information Agency (BIG): Cibinong, Indonesia, 2014.
56. Pangastuti, D.; Sofian, I. Validation of Geoid EGM2008 in Java and Sumatra by the Parameter Mean Dynamic Topography (MDT) on Geometric Geoid. *Maj. Ilm. Globe* **2015**, *17*, 79–88.
57. Hadjimitsis, D.G.; Papadavid, G.; Agapiou, A.; Themistocleous, K.; Hadjimitsis, M.G.; Retalis, A.; Michaelides, S.; Chrysoulakis, N.; Toullos, L.; Clayton, C.R.I. Atmospheric correction for satellite remotely sensed data intended for agricultural applications: Impact on vegetation indices. *Nat. Hazards Earth Syst. Sci.* **2010**, *10*, 89–95.
58. Deer, P.J.; Eklund, P. A study of parameter values for a Mahalanobis Distance fuzzy classifier. *Fuzzy Sets Syst.* **2003**, *137*, 191–213.
59. Xie, X.L.; Beni, G. A validity measure for fuzzy clustering. *IEEE Trans. Pattern Anal. Mach. Intell.* **1991**, *13*, 841–847.
60. Tobias, O.J.; Seara, R. Image Segmentation by Histogram Thresholding Using Fuzzy Sets. *IEEE Trans. Image Process.* **2002**, *11*, 1457–1465.
61. Shi, W.; Liu, K.; Huang, C. A Fuzzy-Topology-Based Area Object Extraction Method. *IEEE Trans. Geosci. Remote Sens.* **2010**, *48*, 147–154.
62. Zhao, X.; Stein, A.; Chen, X. Application of random sets to model uncertainties of natural entities extracted from remote sensing images. *Stoch. Environ. Res. Risk Assess.* **2010**, *24*, 713–723.
63. Leeuw, J.D.; Jia, H.; Yang, L.; Liu, X.; Schmidt, K.; Skidmore, A.K. Comparing accuracy assessments to infer superiority of image classification methods. *Int. J. Remote Sens.* **2006**, *27*, 223–232.
64. Manandhar, R.; Odeh, I.O.A.; Ancev, T. Improving the Accuracy of Land Use and Land Cover Classification of Landsat Data Using Post-Classification Enhancement. *Remote Sens.* **2009**, *1*, 330–344.
65. Foody, G.M. Thematic Map Comparison: Evaluating the Statistical Significance of Differences in Classification Accuracy. *Photogramm. Eng. Remote Sens.* **2004**, *70*, 627–633.
66. Burrough, P.A. Natural object with indeterminate boundaries. In *Geographic Object with Indeterminate Boundaries*; Burrough, P.A., Frank, A.U., Eds.; Taylor & Francis: Abingdon, UK, 1996.
67. Zhao, X.; Stein, A.; Chen, X.; Zhang, X. Quantification of Extensional Uncertainty of Segmented Image Objects by Random Sets. *IEEE Trans. Geosci. Remote Sens.* **2011**, *49*, 2548–2557.

